



CHORUS

This is the accepted manuscript made available via CHORUS. The article has been published as:

Direct Visualization of Gigahertz Acoustic Wave Propagation in Suspended Phononic Circuits

Daehun Lee, Qiyu Liu, Lu Zheng, Xuejian Ma, Huan Li, Mo Li, and Keji Lai

Phys. Rev. Applied **16**, 034047 — Published 28 September 2021

DOI: [10.1103/PhysRevApplied.16.034047](https://doi.org/10.1103/PhysRevApplied.16.034047)

Direct Visualization of Gigahertz Acoustic Wave Propagation in Suspended Phononic Circuits

Daehun Lee^{†1}, Qiyu Liu^{†2}, Lu Zheng¹, Xuejian Ma¹, Huan Li², Mo Li^{*2,3}, Keji Lai^{*1}

¹ Department of Physics, University of Texas at Austin, Austin TX 78712, USA

² Department of Electrical and Computer Engineering, University of Washington, Seattle, WA, 98195, USA

³ Department of Physics, University of Washington, Seattle, WA, 98195, USA

[†] These authors contributed equally to this work

* E-mails: moli96@uw.edu; kejilai@physics.utexas.edu

Abstract

We report direct visualization of gigahertz-frequency Lamb waves propagation in aluminum nitride phononic circuits by transmission-mode microwave impedance microscopy (TMIM). Consistent with the finite-element modeling, the acoustic eigenmodes in both a horn-shaped coupler and a sub-wavelength waveguide are revealed in the TMIM images. Using fast Fourier transform filtering, we quantitatively analyze the acoustic loss of individual Lamb modes along the waveguide and the power coupling coefficient between the waveguide and the parabolic couplers. Our work provides insightful information on the propagation, mode conversion, and attenuation of acoustic waves in piezoelectric nanostructures, which is highly desirable for designing and optimizing phononic devices for microwave signal processing and quantum information transduction.

I. Introduction

Acoustic waves in the radiofrequency (MHz to GHz) range propagate in solid structures with a speed of several km/s that is 5 orders of magnitude slower than speed of light. Therefore, transduction from electromagnetic waves to acoustic waves enables signal processing on a dramatically slower timescale and much reduced device dimensions. Because acoustic waves cannot propagate in vacuum, radiative crosstalk between signal channels in acoustic devices is also much lower than in electromagnetic devices. As a result, various types of acoustic devices, such as surface acoustic wave (SAW), bulk acoustic wave (BAW), and flexural plate wave (FPW) devices, are widely utilized as delay lines, filters, oscillators, convolvers in wireless communication applications [1-3], and mass, pressure, and flow sensors in sensing applications [4]. Recently, propagating acoustic waves are considered universal quantum interconnects between different solid-state qubit systems, e.g., defect centers and superconducting qubits [5-10], for two reasons. First, the quantum states of these systems are highly susceptible to mechanical deformation with high coupling coefficients [11-15]; second, the acoustic wave can propagate with very low loss and noise at low temperatures [16,17]. There is also a strong interest in achieving efficient transduction between optical and microwave photons mediated by acoustic modes in optomechanical systems through acousto-optic coupling [18]. Optical waves and microwave-frequency acoustic (or phononic) modes are confined in wavelength-scale structures and interact through efficient acousto-optic coupling [19-26]. However, direct conversion from optical photons to acoustic phonons is intrinsically low in energy efficiency because of their large disparity in frequency (~ 5 orders of magnitude), assuming the same wavelengths. In contrast, converting MHz-to-GHz electromagnetic waves to acoustic phonons can be achieved much more efficiently using electromechanical transducers on piezoelectric materials [27-29]. To achieve efficient transduction, it is critical to engineer phononic structures to effectively guide and couple acoustic phonons into optomechanical systems.

A major challenge for designing phononic systems is that the density of state of acoustic phonons is very high [30], and different polarization modes inherently couple with each other through geometric deformation. With a high acoustic frequency, the ratio between the phononic structures' dimensions to the acoustic wavelength becomes high, making it computationally expensive to perform a full 3D finite-element simulation. The mechanical properties of materials that are deposited during device fabrication are also more susceptible to fabrication processes

than their optical properties, making simulations less accurate. In order to complement mechanical simulations, experimental probing of the acoustic fields has become an important field of research in recent years. For instance, MHz surface displacement fields have been imaged by scanning laser reflectometry [31,32], pump-probe technique [33,34], homodyne and heterodyne interferometry [35-37], stroboscopic X-ray imaging [38,39], scanning electron microscopy (SEM) [40,41], scanning tunneling microscopy (STM) [42,43], and nonlinear acoustic force microscopy (AFM) [44]. However, none of these techniques can simultaneously achieve sub-100 nm spatial resolution and > 1 GHz operation frequency, which are crucial for wavelength-scale acousto-optic devices. Thus, a method that allows nanoscale investigation of wave phenomena, such as interference, diffraction, and localization, of GHz acoustic waves is desirable for designing and optimizing efficient optomechanical systems.

In this work, we report the visualization of 3.44 GHz Lamb waves in suspended aluminum nitride (AlN) phononic waveguides by transmission-mode microwave impedance microscopy (TMIM) [45,46]. The imaging results vividly demonstrate the coupling from anti-symmetrical membrane modes to waveguide modes through a parabolic horn-shaped coupler. Using fast Fourier transform (FFT) filtering, we identify individual waveguide modes and analyze their propagation loss along the waveguide. Our work provided insightful information on the propagation, attenuation, and coupling of Lamb waves in phononic circuits, which cannot be obtained by traditional microwave network analysis.

II. Device and Simulation

The suspended phononic circuits in this work are fabricated on *c*-axis polycrystalline AlN thin films (thickness $t = 330$ nm) grown by magnetron sputtering on SiO₂/Si wafers. The circuit consists of an acoustic waveguide with width $w = 1$ μm and length $L = 100$ μm , connected to two identical parabolic horn-shaped acoustic couplers [47,48] with a length of $L_h = 100$ μm . The couplers are designed to focus acoustic waves to the waveguide from two interdigital transducers (IDTs), one used as a transmitter and one as a receiver. The waveguide and couplers are patterned by standard electron beam lithography (EBL) and plasma etching of AlN, using 240-nm-thick SiO₂ as the hard mask. The IDT fingers have an aperture width of $A = 20$ μm . They are fabricated with EBL and the deposition of 7 nm Cr and 100 nm Au, followed by a standard lift-off process. To reduce the acoustic loss due to internal reflection and destructive interference in

the IDT region, we use the split-finger design with a period of $3\ \mu\text{m}$ and 4 fingers per period (inset of Fig. 1a). The 3rd harmonic mode with $\lambda = 1\ \mu\text{m}$ excited by this IDT is the Lamb wave to be investigated below. Another layer of 7 nm Cr / 300 nm Au is deposited to thicken the bonding pads. Finally, the $3\ \mu\text{m}$ thermal SiO_2 underneath the AlN film is removed using a vapor HF etcher to release the device from the substrate.

Electrical characterization of the AlN phononic circuit is carried out with a vector network analyzer (VNA). The transmitter and receiver IDTs are connected to the VNA through microwave cables and a pair of RF probes. The measured reflection coefficient (S_{11}) spectrum (Fig. 1b) shows a resonance at $f = 3.44\ \text{GHz}$, which corresponds to the excitation of the Lamb mode at $\lambda = 1\ \mu\text{m}$. The transmission coefficient (S_{21}) spectrum (Fig. 1c) between the two IDTs shows a smaller peak at the same frequency, indicating transmission of the Lamb wave through the circuit. Note that the S_{21} spectrum shows a few ripples, which can be attributed to the reflection and interference of the acoustic wave and the RF crosstalk between the input and output IDT ports. The capacitive crosstalk background signal has been subtracted for clarity.

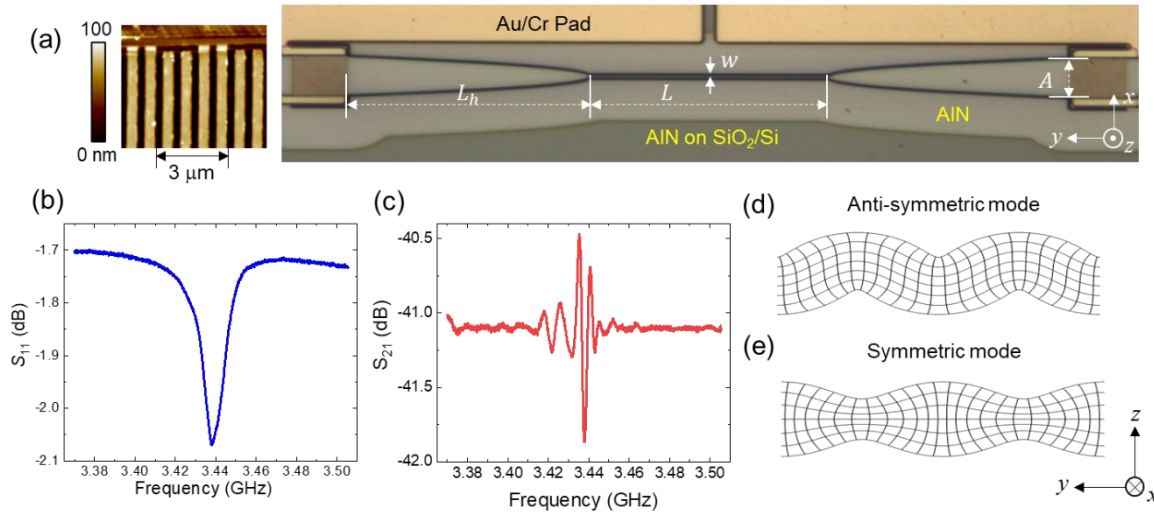


FIG. 1 (a) Optical image of the AlN phononic circuits. The inset on the left shows the AFM image of the split-finger IDT. (b) S_{11} and (c) S_{21} spectra of the device measured by a VNA, showing the acoustic resonance at $f = 3.44\ \text{GHz}$. (d) Simulation results plotted in deformed grids showing the anti-symmetric (A-mode) and (e) symmetric (S-mode) modes of the free-standing membrane at the IDT region.

To understand the excited Lamb mode, we model the IDT region as a large AlN membrane and simulate with the finite-element method (FEM). Figs. 1d and 1e show the simulated fundamental modes plotted in deformed grids, where the displacement fields are either

anti-symmetric (A-mode) or symmetric (S-mode) with respect to the xy -plane. Because the IDTs are patterned only on the top surface of the membrane, the electric fields generated by the IDTs are asymmetric along the thickness of the membrane. Consequently, the anti-symmetric membrane modes are predominantly excited. Therefore, the observed resonance at 3.44 GHz is attributed to the anti-symmetric Lamb mode, which agrees with the simulation results.

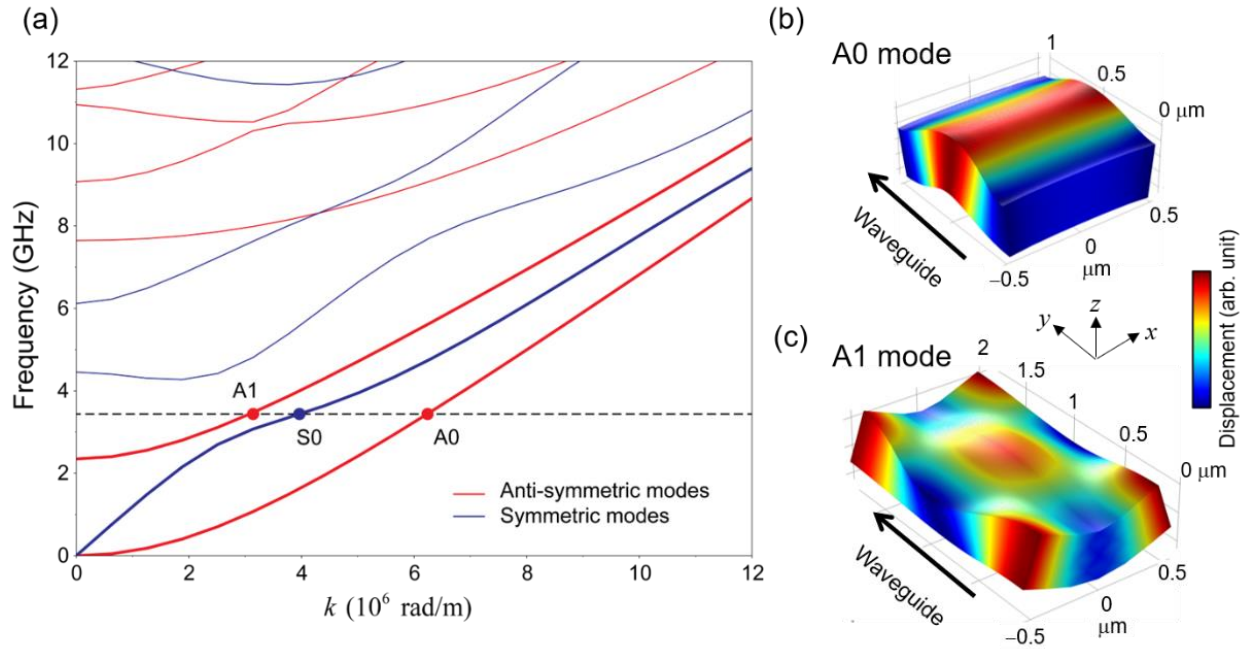


FIG. 2. (a) Calculated dispersion relation of a free-standing AlN phononic waveguide with $1 \mu\text{m}$ width. The red and blue curves represent anti-symmetric and symmetric modes, respectively. The intersection points between the dashed line at $f = 3.44 \text{ GHz}$ and three lowest branches of the dispersion curves are labeled as A0, S0, and A1 (see text). (b) 3D simulation results showing the mode shape of A0 and (c) A1 modes with color indicating the displacement magnitude.

Compared with the membrane modes discussed above, which are only confined in the z -direction, the acoustic wave propagating in the suspended AlN circuits is also confined in the transverse x -direction. In the following, we will denote the Lamb modes in the subwavelength waveguide as waveguide modes. Fig. 2a shows the simulated dispersion relation of various modes on a waveguide with a width of $1 \mu\text{m}$ and a thickness of 330 nm . The dashed line denoted the excitation frequency at 3.44 GHz , which intersects with three branches of dispersion curves of the waveguide modes, hereafter labeled as S0, A1, and A0, respectively. Due to symmetry matching, the anti-symmetric membrane mode excited by the IDTs can only couple to the A0 and A1 modes. Fig. 2b and c display the simulated displacement fields of the two anti-symmetric

modes (A0 and A1). Here the A0 mode in the lowest acoustic branch is the fundamental anti-symmetric breathing mode with $\lambda = 1 \mu\text{m}$, where the displacement field is uniformly distributed in the cross-section (xz plane). A1 with $\lambda = 2 \mu\text{m}$ is the first-order anti-symmetric mode, where the displacement is out of phase between the center of the waveguide and the boundary of the waveguide. Detailed simulation results of the A0, S0, and A1 modes are included in Appendix A.

III. Experimental Results

Imaging of Lamb waves on the phononic circuit is carried out in our TMIM setup, an atomic-force-microscopy (AFM)-based technique with sub-100nm spatial resolution [45,46]. Fig. 3a shows the configuration of the TMIM experiment, where the acoustic wave is launched by the emitter IDT and the induced surface potential modulation at GHz is detected by the tip. The signal is then amplified and demodulated by an in-phase/quadrature (I/Q) mixer, using the same microwave source as the reference signal. The time-varying acoustic signal is thus converted to time-independent TMIM images, which are simultaneously acquired as the topographic image during the scanning (Appendix B). For simplicity, we will only present one of the two orthogonal TMIM channels in the following discussion.

Fig. 3b shows the SEM image of the AlN phononic circuit, where TMIM images were taken in several $10\mu\text{m} \times 10\mu\text{m}$ areas marked by dashed boxes. Near the emitter IDT, the acoustic pattern in Fig. 3c contains a substantial portion of left-moving waves. The corresponding 2D FFT spectral image is shown in Fig. 3d. The large diffusive spots near the center of FFT data correspond to slow-varying background signals in the real space, presumably due to incoherent motion of the membrane. By filtering out this feature (Fig. 3e), one can see that the highest FFT intensity lies along the propagation direction (y axis) with a wavevector $|k| = 2\pi \cdot 1 \mu\text{m}^{-1}$, consistent with $\lambda = 2\pi/k = 1 \mu\text{m}$ of the anti-symmetric membrane mode. From the inverse FFT image in Fig. 3f, it is nevertheless obvious that Lamb waves with the same $|k|$ along other in-plane directions are present because of multiple reflections from boundaries of the parabolic coupler. At the bottom of this parabola (Fig. 3g), the wave front is strongly curved. Correspondingly, while the Lamb wave retains the wavevector $|k| = 2\pi \cdot 1 \mu\text{m}^{-1}$, the FFT intensity in the y -direction drops to zero (Fig. 3h). Finally, in the other parabolic coupler near the exit side of the waveguide, Lamb wave with the same $|k|$ but a much weaker amplitude is observed, as evidenced from both the raw and the FFT-filtered TMIM images (Fig. 3k – 3n).

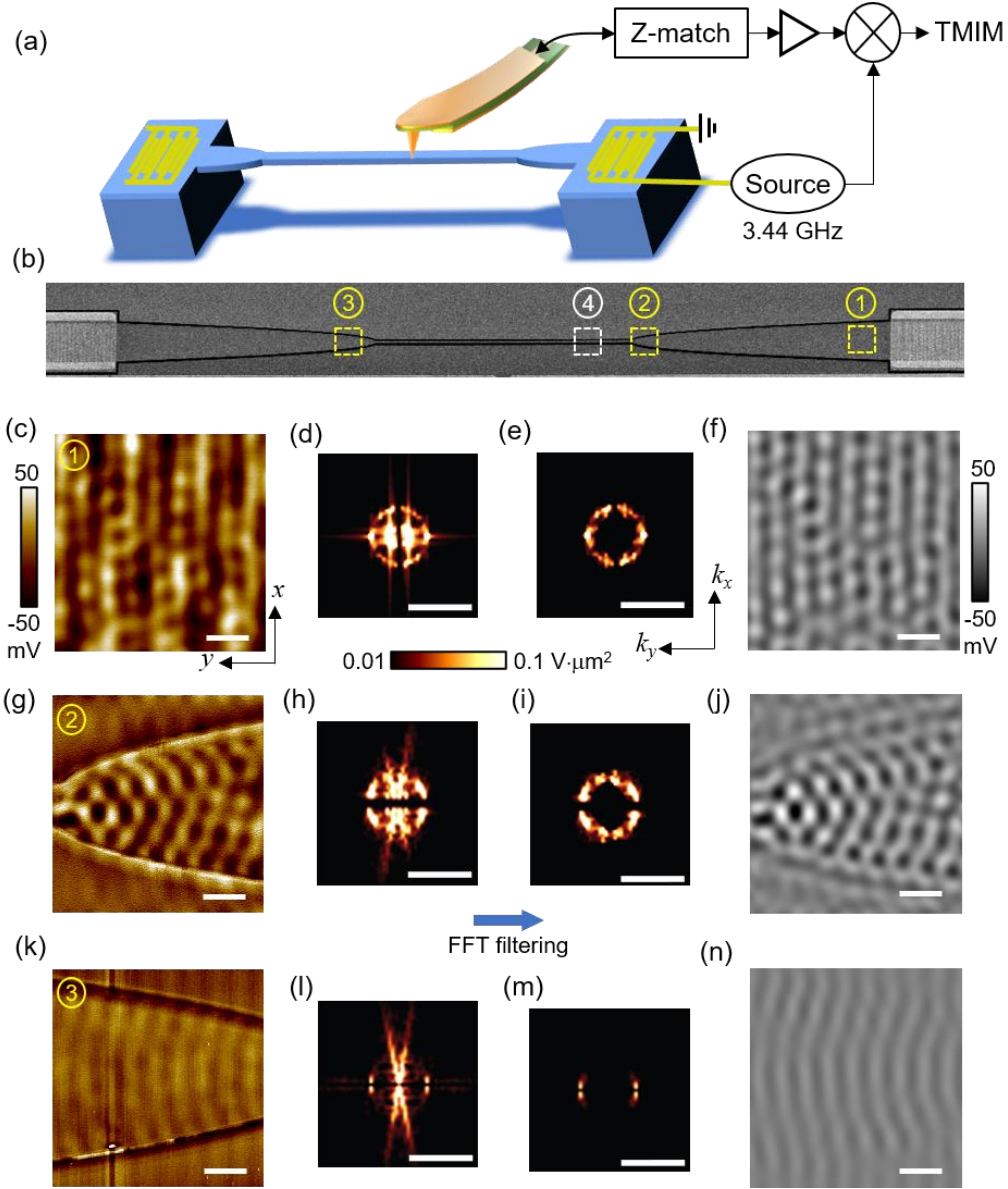


FIG. 3. (a) Schematics of the suspended phononic circuit and the TMIM setup. (b) SEM image of the device. The four dashed boxes show the locations where TMIM images are acquired. (c) TMIM image and (d) 2D FFT spectral image in Box #1. (e) FFT image after removing the diffusive spots at the center. (f) Inverse FFT image of (e). (g – j) Same as (c – e) in Box #2. (k – n) Same as (c – e) in Box #3. Scale bars are $2 \mu\text{m}$ for real-space images and $2\pi \cdot 2 \mu\text{m}^{-1}$ for k -space FFT images. The false-color scales for panels (c, g, k) are the same, so are (d, e, h, i, l, m), and (f, j, n).

We now focus our attention on acoustic modes in the suspended phononic waveguide and compare the results with FEM simulation in Fig. 2. Fig. 4a shows the TMIM image taken in Box #4, where a complex waveform of the surface potential is clearly observed. By taking FFT (Fig. 4b) of the raw data, one can see that the TMIM results are a superposition of three distinct harmonic components. The fringe-like pattern along the k_x direction in the FFT spectrum (Fig. 4d)

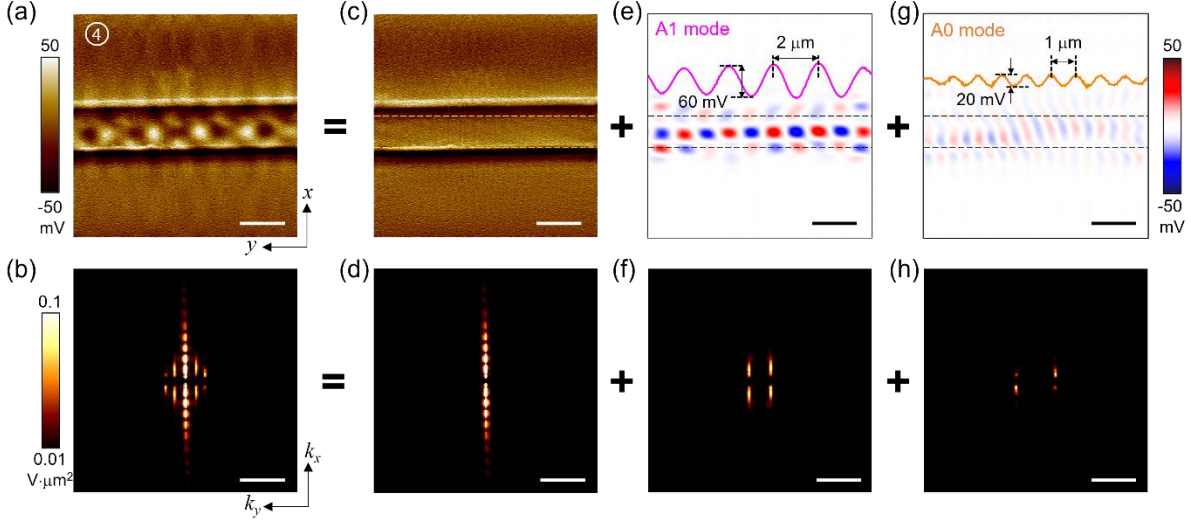


FIG. 4. **(a)** TMIM image and **(b)** its 2D FFT spectral image in Box #4 in Fig. 3b. **(c)** Filtered TMIM and **(d)** FFT images of the topographic artifact due to tranches on both sides of the waveguide. **(e)** Filtered TMIM and **(f)** FFT images associated with the A1 mode. **(g)** Filtered TMIM and **(h)** FFT images associated with the A0 mode. Insets of (e) and (g) show line cuts through center of the images. Note that (a) is the superposition of (c, e, g) in the real space and (b) the superposition of (d, f, h) in the k -space. Scale bars are $2 \mu\text{m}$ for real-space images and $2\pi \cdot 2 \mu\text{m}^{-1}$ for k -space FFT images.

corresponds to the double-slit feature in the TMIM image (Fig. 4c), which is from horizontal boundaries of the waveguide. Because of the finite size of the AFM tip, the waveguide appears to be slightly wider in the TMIM image than its actual width of $1 \mu\text{m}$. Other than this topographic crosstalk, the most prominent FFT features are the four bright lines at $|k_y| = 2\pi \cdot 0.5 \mu\text{m}^{-1}$ (Fig. 4f). The inverse FFT image in Fig. 4e reveals that they are associated with the A1 mode with out-of-phase motion between the center and boundary of the waveguide, as depicted in Fig. 2c. Note that the signals outside the suspended nanobeam in Fig. 4e are due to both FFT filtering of the eigenmode profile (Fig. 2c) and topographic artifact when the tip plunges into the grooves on each side of the waveguide. Finally, the FFT image also display weak but discernible features at $|k_y| = 2\pi \cdot 1 \mu\text{m}^{-1}$ (Fig. 4h). The corresponding real-space image in Fig. 4g suggests that this is the A0 mode with in-phase particle motion across the width of the waveguide (Fig. 2b). The line profiles through the center of Figs. 4e and 4g are plotted in the corresponding insets, showing $\lambda = 2 \mu\text{m}$ and $1 \mu\text{m}$ for the two modes, respectively. By comparing the amplitudes of the two modes, it is obvious that the A1 mode is the dominant mode excited in the waveguide. In other words, the anti-symmetric membrane mode in the parabolic coupler is mostly converted to the

A1 mode in the waveguide, presumably due to mode conversion occurring near the tip of the parabolic coupler where the wavefront is distorted from the planar wavefront from the IDT (Fig. 3g-j). This conversion is undesired for many applications where the A0 mode in the waveguide is preferred [26]. Therefore, a better design of the coupler will be needed and the TMIM measurement can provide critical insights.

The FFT filtering method described above allows us to remove the topographic crosstalk from the TMIM data and analyze oscillating amplitudes of individual waveguide modes. Figs. 5a and 5b plot the TMIM signals of A1 and A0 mode through the 100 μm long suspended waveguide, respectively. Representative FFT-filtered images are also shown near the entrance and exit points of the waveguide. For the primary A1 mode, the amplitude drops by a factor of ~ 1.5 over a length of 100 μm . The acoustic power loss is thus ~ 35 dB/mm, which is reasonable for the narrow waveguide. On the other hand, the decay of A0 mode is smaller ~ 20 dB/mm [26], although the error bar is large due to the weak signals and distorted wave profiles.

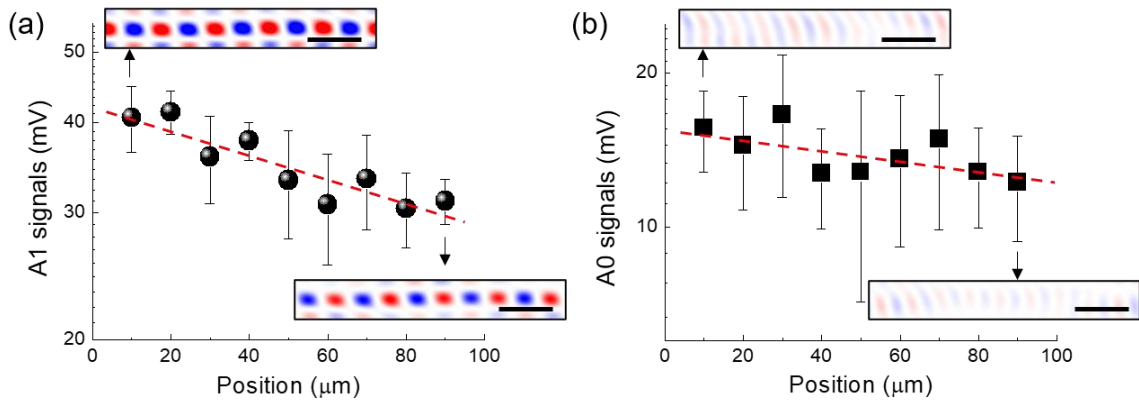


FIG. 5. (a) TMIM signals of the A1 and (b) A0 modes along the 100 μm waveguide. The insets show the filtered TMIM images associated with the A1 and A0 modes near the entrance and exit points of the waveguide. The red dashed lines are linear fits to the semi-log plots. All scale bars are 2 μm .

IV. Discussions

Quantitative analysis of the TMIM results reveals important information about the acoustic mode evolution in the suspended phononic circuit that cannot be obtained by two-port measurements. The S_{21} data in Fig. 1c, for instance, convolve the piezoelectric and inverse piezoelectric transduction at the two IDTs, the acoustic propagation in the two parabolic couplers, and mode conversion in and out of the waveguide. In contrast, the TMIM imaging and FFT filtering allow us to focus on the waveguide modes and extract their acoustic loss in the narrow

waveguide. The imaging method also reveals the acoustic mode coupling between the parabolic horn and the waveguide. When the Lamb wave enters the waveguide, the TMIM peak-to-peak signal drops from ~ 100 mV on the coupler side (Fig. 3g) to ~ 60 mV in the waveguide (Fig. 4e). Since the acoustic power is proportional to the square of oscillation amplitude and the width of the free-standing film, we can calculate a power coupling coefficient of $\sim 20\%$ by assuming a ratio of 2:1 in effective width near the entrance point. After the propagation of $100 \mu\text{m}$, the TMIM signal drops to ~ 40 mV at the end of the waveguide. Using the same coupling coefficient, one can estimate a TMIM signal of $10 \sim 15$ mV when entering the left parabolic coupler, consistent with the measured data in Fig. 3k. From the measured S_{21} of ~ -40 dB, we obtain an electromechanical power conversion factor of $6 \sim 7\%$ at the IDTs, which matches well with that of typical IDTs on AlN membranes [21,22,26]. As a result, the TMIM experiment provides a quantitative picture of various components in the phononic device down to the sub-wavelength scale.

Our work in visualizing GHz Lamb waves exemplifies the ability of TMIM to perform highly sensitive nanoscale acoustic imaging. From the calculated electromechanical power coupling efficiency, one can estimate the mechanical oscillation amplitude of 10 pm under an input power of 10 mW to the IDT (Appendix C). Furthermore, the good signal-to-noise ratio in the TMIM images indicates that the detection limit at a normal scan rate of 10 min per frame is on the order of 0.1 pm. This level of surface acoustic vibration is extremely challenging for scanning laser interferometry [33,34], stroboscopic X-ray imaging [38,39], and nonlinear acoustic force microscopy [44]. More importantly, at the operation frequency of ~ 3 GHz, the acoustic wavelength of $1 \sim 2 \mu\text{m}$ is too small for optics-based techniques whose spatial resolution is diffraction limited. The AFM-based TMIM experiment, on the other hand, can routinely resolve sub- 100nm features in the acoustic imaging. For even higher frequencies in the 10 GHz regime, which is of critical importance for optomechanics and quantum acoustics, TMIM might be the only technique of choice to map out the acoustic patterns on complex device structures [46].

V. Conclusion

To summarize, we report the fabrication of suspended AlN acoustic waveguides and the visualization of 3.44 GHz Lamb waves on such phononic devices. Combining finite-element modeling and transmission-mode microwave microscopy, we are able to identify the membrane

and waveguide modes and quantitatively analyze the acoustic coupling between the sub-wavelength waveguide and a pair of parabolic couplers. The FFT filtering allows us to separate the contribution from the two eigenmodes of the waveguide and calculate their acoustic loss. Our work demonstrates the exquisite sensitivity and high resolution of the TMIM technique, which is expected to find future applications in electromechanics, optomechanics, and quantum science and engineering.

ACKNOWLEDGMENTS

The TMIM work was supported by NSF Division of Materials Research Award DMR-2004536 and Welch Foundation Grant F-1814. The data analysis was partially supported by the NSF through the Center for Dynamics and Control of Materials, an NSF Materials Research Science and Engineering Center (MRSEC) under Cooperative Agreement DMR-1720595. The phononic waveguide work was supported by NSF Award EFMA-1741656 and EFMA-1641109. Part of this work was conducted at the Washington Nanofabrication Facility / Molecular Analysis Facility, a National Nanotechnology Coordinated Infrastructure (NNCI) site at the University of Washington with partial support from the National Science Foundation via awards NNCI-1542101 and NNCI-2025489.

APPENDIX A: Finite-element modeling of the waveguide modes

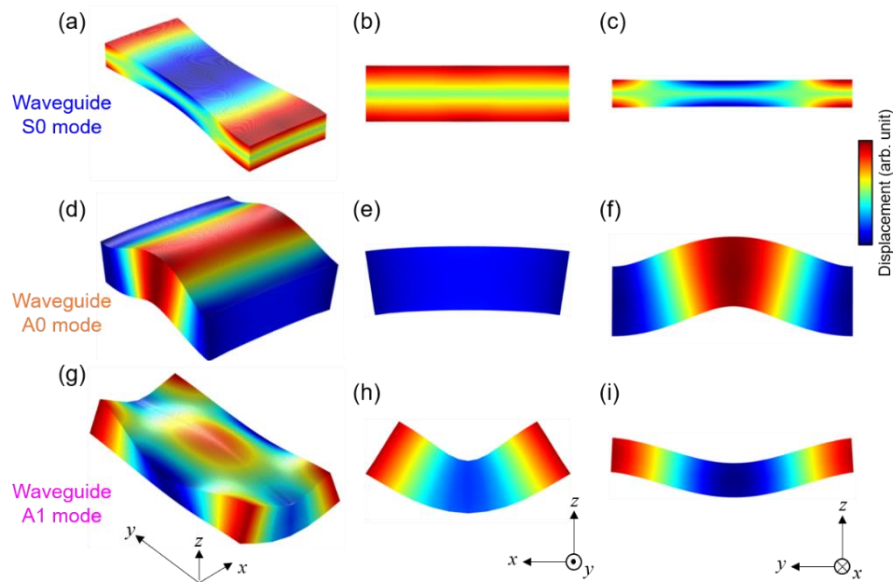


FIG. 6. Finite-element modeling results of the **(a-c)** S0, **(d-f)** A0, and **(g-i)** A1 modes the suspended AlN waveguide (330 nm in thickness and 1 μm in width). Panels (a, d, g) are the 3D views. Panels (b, e, h) are projections in the xz -plane. Panels (c, f, i) are projections in the yz -plane. Periodic boundary conditions are used for the xz -plane and free moving boundary for the xy - and yz -planes.

APPENDIX B: AFM and TMIM images in a large field of view

Fig. 7 shows the simultaneously acquired AFM and TMIM images of the AlN waveguide device in a large field of view. The I/Q mixer in the TMIM electronics generates two orthogonal output channels, as displayed in Figs. 7b and 7c. The total TMIM signals, as plotted in Fig. 5, are vector sum of signals from the two channels. A plot of the TMIM-2 signal in Fig. 7d along the center of the waveguide shows the small decay of acoustic waves.

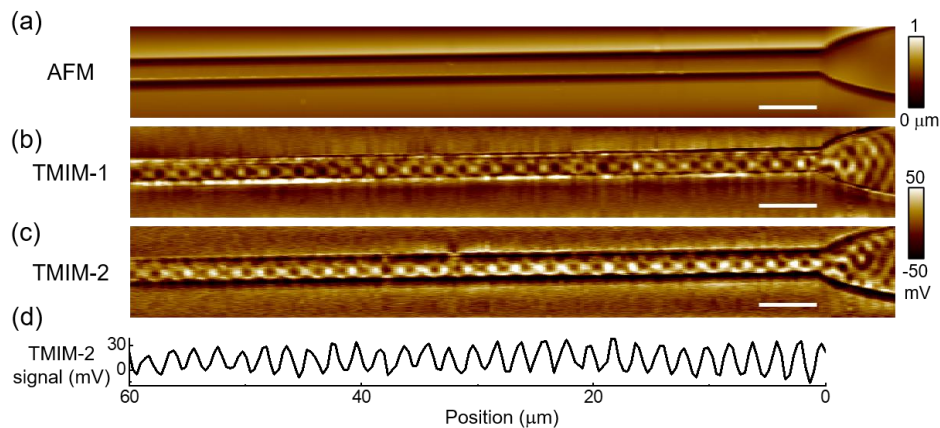


FIG. 7. **(a)** AFM, **(b)** TMIM-1, and **(c)** TMIM-2 images in a large field of view. Scale bars are 5 μm . **(d)** TMIM-2 signals along the center of the waveguide in (c).

APPENDIX C: FEM simulation of the surface displacements and electric potential.

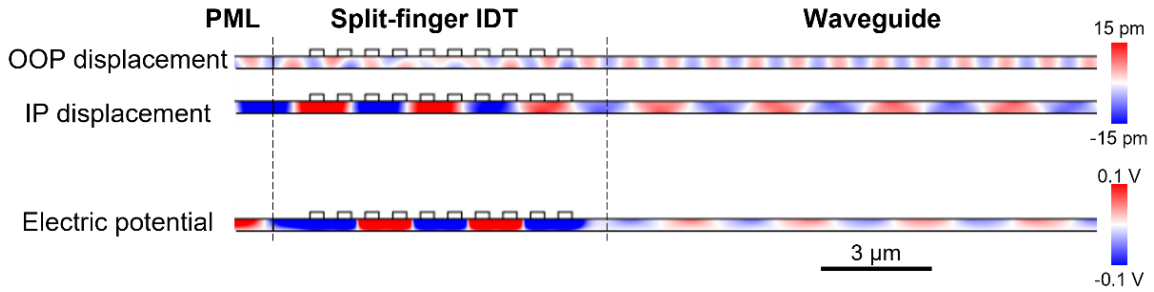


Fig. 8. Simulated displacement fields and electric potential on the suspended AlN membrane device under ± 1 V excitation or ~ 10 mV input power at the split-finger IDT. The mechanical oscillation amplitude is on the order of 10 pm. Both out-of-plane and in-plane displacements contribute to the surface potential through different piezoelectric components (d_{33} and d_{31}) of the c -axis polycrystalline AlN membrane. OOP: out-of-plane; IP: in-plane; PML: perfectly matching layer.

References:

- [1] C. Campbell, Surface acoustic wave devices for mobile and wireless communications (Academic Press, San Diego, 1998), Applications of modern acoustics.
- [2] K.-Y. Hashimoto, Surface acoustic wave devices in telecommunications : modelling and simulation (Springer, Berlin ; New York, 2000).
- [3] D. P. Morgan, Surface acoustic wave filters : with applications to electronic communications and signal processing (Academic Press, Amsterdam ; London, 2007), 2nd edn.
- [4] D. Ballantine Jr, R. M. White, S. J. Martin, A. J. Ricco, E. Zellers, G. Frye, and H. Wohltjen, Acoustic wave sensors: theory, design and physico-chemical applications (Elsevier, 1996).
- [5] M. V. Gustafsson, T. Aref, A. F. Kockum, M. K. Ekstrom, G. Johansson, and P. Delsing, Propagating phonons coupled to an artificial atom, Science 346, 207 (2014).
- [6] M. J. A. Schuetz, E. M. Kessler, G. Giedke, L. M. K. Vandersypen, M. D. Lukin, and J. I. Cirac, Universal Quantum Transducers Based on Surface Acoustic Waves, Physical Review X 5, 031031 (2015).
- [7] Y. Chu, P. Kharel, W. H. Renninger, L. D. Burkhardt, L. Frunzio, P. T. Rakich, and R. J. Schoelkopf, Quantum acoustics with superconducting qubits, Science 358, 199 (2017).
- [8] A. Noguchi, R. Yamazaki, Y. Tabuchi, and Y. Nakamura, Qubit-Assisted Transduction for a Detection of Surface Acoustic Waves near the Quantum Limit, Phys. Rev. Lett. 119, 180505 (2017).
- [9] M. K. Ekström, T. Aref, J. Runeson, J. Björck, I. Boström, and P. Delsing, Surface acoustic wave unidirectional transducers for quantum applications, Appl. Phys. Lett. 110, 073105 (2017).
- [10] B. A. Moores, L. R. Sletten, J. J. Viennot, and K. W. Lehnert, Cavity Quantum Acoustic Device in the Multimode Strong Coupling Regime, Phys. Rev. Lett. 120, 227701 (2018).
- [11] E. R. MacQuarrie, T. A. Gosavi, N. R. Jungwirth, S. A. Bhave, and G. D. Fuchs, Mechanical Spin Control of Nitrogen-Vacancy Centers in Diamond, Phys. Rev. Lett. 111, 227602 (2013).

- [12] P. Ouartchaiyapong, K. W. Lee, B. A. Myers, and A. C. Jayich, Dynamic strain-mediated coupling of a single diamond spin to a mechanical resonator, *Nat Commun* 5, 4429 (2014).
- [13] D. A. Golter, T. Oo, M. Amezcua, K. A. Stewart, and H. Wang, Optomechanical Quantum Control of a Nitrogen-Vacancy Center in Diamond, *Phys. Rev. Lett.* 116, 143602 (2016).
- [14] K. W. Lee, D. Lee, P. Ouartchaiyapong, J. Minguzzi, J. R. Maze, and A. C. B. Jayich, Strain Coupling of a Mechanical Resonator to a Single Quantum Emitter in Diamond, *Physical Review Applied* 6, 034005 (2016).
- [15] S. Meesala, Y. I. Sohn, B. Pingault, L. Shao, H. A. Atikian, J. Holzgrafe, M. Gundogan, C. Stavrakas, A. Sipahigil, C. Chia, R. Evans, M. J. Burek, M. Zhang, L. Wu, J. L. Pacheco, J. Abraham, E. Bielejec, M. D. Lukin, M. Atature and M. Loncar, Strain engineering of the silicon-vacancy center in diamond, *Phys. Rev. B* 97, 205444 (2018).
- [16] R. Manenti, M. J. Peterer, A. Nersisyan, E. B. Magnusson, A. Patterson, and P. J. Leek, Surface acoustic wave resonators in the quantum regime, *Phys. Rev. B* 93, 041411 (R) (2016).
- [17] E. B. Magnusson, B. H. Williams, R. Manenti, M. S. Nam, A. Nersisyan, M. J. Peterer, A. Ardavan, and P. J. Leek, Surface acoustic wave devices on bulk ZnO crystals at low temperature, *Appl. Phys. Lett.* 106, 063509 (2015).
- [18] M. Mirhosseini, A. Sipahigil, M. Kalaei, and O. Painter, Superconducting qubit to optical photon transduction, *Nature* 588, 599 (2020).
- [19] F. M. Mayor, W. Jiang, C. J. Sarabalis, T. P. McKenna, J. D. Witmer, and A. H. Safavi-Naeini, Physical Review Applied 15, Gigahertz Phononic Integrated Circuits on Thin-Film Lithium Niobate on Sapphire, *Physical Review Applied* 15, 014039 (2021)
- [20] W. Fu, Z. Shen, Y. Xu, C. L. Zou, R. Cheng, X. Han, and H. X. Tang, Phononic integrated circuitry and spin-orbit interaction of phonons, *Nat Commun* 10, 2743 (2019).
- [21] H. Li, Q. Liu, and M. Li, Electromechanical Brillouin scattering in integrated planar photonics, *APL Photonics* 4, 080802 (2019).
- [22] H. Li, S. A. Tadesse, Q. Liu, and M. Li, Nanophotonic cavity optomechanics with propagating acoustic waves at frequencies up to 12 GHz, *Optica* 2, 826 (2015).
- [23] E. A. Kittlaus, H. Shin, and P. T. Rakich, Large Brillouin amplification in silicon, *Nat. Photon.* 10, 463 (2016).
- [24] H. Shin, W. Qiu, R. Jarecki, J. A. Cox, R. H. Olsson, 3rd, A. Starbuck, Z. Wang, and P. T. Rakich, Tailorable stimulated Brillouin scattering in nanoscale silicon waveguides, *Nat Commun* 4, 1944 (2013).
- [25] A. H. Safavi-Naeini, D. Van Thourhout, R. Baets, and R. Van Laer, Controlling phonons and photons at the wavelength scale: integrated photonics meets integrated phononics, *Optica* 6, 213 (2019).
- [26] Q. Y. Liu, H. Li, and M. Li, Electromechanical Brillouin scattering in integrated optomechanical waveguides, *Optica* 6, 778 (2019).
- [27] K. Yamanouchi and Y. Satoh, Ultra Low-Insertion-Loss Surface Acoustic Wave Filters Using Unidirectional Interdigital Transducers with Grating SAW Substrates, *Jpn. J. Appl. Phys.* 44 4532 (2005).

- [28] W. Jiang, C. J. Sarabalis, Y. D. Dahmani, R. N. Patel, F. M. Mayor, T. P. McKenna, R. Van Laer, and A. H. Safavi-Naeini, Efficient bidirectional piezo-optomechanical transduction between microwave and optical frequency, *Nat. Commun.* 11, 1166 (2020).
- [29] X. Han, W. Fu, C. Zhong, C.L. Zou, Y. Xu, A.A. Sayem, M. Xu, S. Wang, R. Cheng, L. Jiang, and H. X. Tang, Cavity piezo-mechanics for superconducting-nanophotonic quantum interface, *Nat. Commun.* 11, 3237 (2020).
- [30] M. S. Kushwaha, P. Halevi, L. Dobrzynski, and B. Djafari-Rouhani, Acoustic band structure of periodic elastic composites, *Phys. Rev. Lett.* 71, 2022 (1993).
- [31] A. Mahjoubfar, K. Goda, A. Ayazi, A. Fard, S. H. Kim, and B. Jalali, High-speed nanometer-resolved imaging vibrometer and velocimeter, *Appl. Phys. Lett.* 98, 101107 (2011).
- [32] Y. Xu, W. Fu, C.-l. Zou, Z. Shen, and H. X. Tang, High quality factor surface Fabry-Perot cavity of acoustic waves, *Appl. Phys. Lett.* 112, 073505 (2018).
- [33] Y. Sugawara, O. Wright, O. Matsuda, M. Takigahira, Y. Tanaka, S. Tamura, and V. Gusev, Watching Ripples on Crystals, *Phys. Rev. Lett.* 88, 185504 (2002).
- [34] D. M. Profunser, O. B. Wright, and O. Matsuda, Imaging Ripples on Phononic Crystals Reveals Acoustic Band Structure and Bloch Harmonics, *Phys. Rev. Lett.* 97, 055502 (2006).
- [35] K. Kokkonen and M. Kaivola, Scanning heterodyne laser interferometer for phase-sensitive absolute-amplitude measurements of surface vibrations, *Appl. Phys. Lett.* 92, 063502 (2008).
- [36] K.-Y. Hashimoto, K. Kashiwa, N. Wu, T. Omori, M. Yamaguchi, O. Takano, S. Meguro, and K. Akahane, A laser probe based on a sagnac interferometer with fast mechanical scan for RF surface and bulk acoustic wave devices, *IEEE transactions on ultrasonics, ferroelectrics, and frequency control* 58, 187 (2011).
- [37] Z. Shen, X. Han, C.-L. Zou, and H. X. Tang, Phase sensitive imaging of 10 GHz vibrations in an AlN microdisk resonator, *Rev. Sci. Instrum.* 88, 123709 (2017).
- [38] R. Whatmore, P. Goddard, B. Tanner, and G. Clark, Direct imaging of travelling Rayleigh waves by stroboscopic X-ray topography, *Nature* 299, 44 (1982).
- [39] E. Zolotoyabko, D. Shilo, W. Sauer, E. Pernot, and J. Baruchel, Visualization of 10 μm surface acoustic waves by stroboscopic x-ray topography, *Appl. Phys. Lett.* 73, 2278 (1998).
- [40] D. Roshchupkin, T. Fournier, M. Brunel, O. Plotitsyna, and N. Sorokin, Scanning electron microscopy observation of excitation of the surface acoustic waves by the regular domain structures in the LiNbO_3 crystals, *Appl. Phys. Lett.* 60, 2330 (1992).
- [41] D. Roshchupkin, M. Brunel, R. Tucoulou, E. Bigler, and N. Sorokin, Reflection of surface acoustic waves on domain walls in a LiNbO_3 crystal, *Appl. Phys. Lett.* 64, 164 (1994).
- [42] W. Rohrbeck, E. Chilla, H.-J. Fröhlich, and J. Riedel, Detection of surface acoustic waves by scanning tunneling microscopy, *Appl. Phys. A* 52, 344 (1991).
- [43] E. Chilla, W. Rohrbeck, H. J. Fröhlich, R. Koch, and K. Rieder, Probing of surface acoustic wave fields by a novel scanning tunneling microscopy technique: Effects of topography, *Appl. Phys. Lett.* 61, 3107 (1992).

- [44] T. Hesjedal, Surface acoustic wave-assisted scanning probe microscopy—a summary, *Rep. Prog. Phys.* 73, 016102 (2009).
- [45] L. Zheng, D. Wu, X. Wu, and K. Lai, Visualization of Surface-Acoustic-Wave Potential by Transmission-Mode Microwave Impedance Microscopy, *Physical Review Applied* 9, 061002 (2018).
- [46] L. Zheng, L. Shao, M. Loncar, and K. Lai, Imaging Acoustic Waves by Microwave Microscopy: Microwave Impedance Microscopy for Visualizing Gigahertz Acoustic Waves, *IEEE Microwave Magazine* 21, 60 (2020).
- [47] I. Yao, High-Performance Elastic Convolver with Parabolic Horns, in *1980 Ultrasonics Symposium (IEEE, 1980)*, pp. 37.
- [48] M. M. de Lima Jr and P. V. Santos, Modulation of photonic structures by surface acoustic waves, *Rep. Prog. Phys.* 68, 1639 (2005).